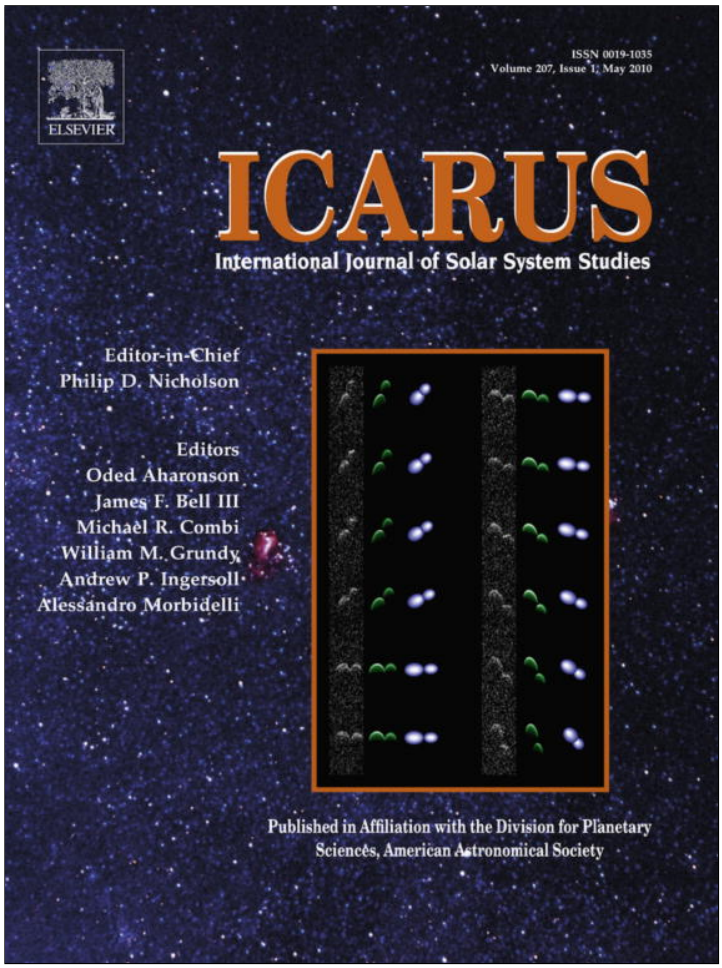

Icarus 207 (2010) 433–447

Contents lists available at ScienceDirect

Icarus

journal homepage: www.elsevier.com/locate/icarus

Aegaeon (Saturn LIII), a G-ring object ☆

M.M. Hedman [a,*], N.J. Cooper [b], C.D. Murray [b], K. Beurle [b], M.W. Evans [b,a], M.S. Tiscareno [a], J.A. Burns [a,c]

[a] Department of Astronomy, Cornell University, Ithaca, NY 14853, USA
[b] Queen Mary University of London, Astronomy Unit, School of Mathematical Sciences, Mile End Road, London E1 4NS, UK
[c] Department of Theoretical and Applied Mechanics, Cornell University, Ithaca, NY 14853, USA

ARTICLE INFO

Article history:
Received 29 July 2009
Revised 28 October 2009
Accepted 29 October 2009
Available online 10 November 2009

Keywords:
Saturn, Satellites
Saturn, Rings
Satellites, Dynamics
Resonances, Orbital

ABSTRACT

Aegaeon (Saturn LIII, S/2008 S1) is a small satellite of Saturn that orbits within a bright arc of material near the inner edge of Saturn's G-ring. This object was observed in 21 images with Cassini's Narrow-Angle Camera between June 15 (DOY 166), 2007 and February 20 (DOY 051), 2009. If Aegaeon has similar surface scattering properties as other nearby small saturnian satellites (Pallene, Methone and Anthe), then its diameter is approximately 500 m. Orbit models based on numerical integrations of the full equations of motion show that Aegaeon's orbital motion is strongly influenced by multiple resonances with Mimas. In particular, like the G-ring arc it inhabits, Aegaeon is trapped in the 7:6 corotation eccentricity resonance with Mimas. Aegaeon, Anthe and Methone therefore form a distinctive class of objects in the Saturn system: small moons in corotation eccentricity resonances with Mimas associated with arcs of debris. Comparisons among these different ring-arc systems reveal that Aegaeon's orbit is closer to the exact resonance than Anthe's and Methone's orbits are. This could indicate that Aegaeon has undergone significant orbital evolution via its interactions with the other objects in its arc, which would be consistent with the evidence that Aegaeon's mass is much smaller relative to the total mass in its arc than Anthe's and Methone's masses are.

1. Introduction

Beginning in early 2004, images from the cameras onboard the Cassini spacecraft revealed the existence of several previously unknown small saturnian satellites: Methone, Pallene, Polydeuces, Daphnis and Anthe (Porco et al., 2005; Murray et al., 2005; Spitale et al., 2006; Cooper et al., 2008). Two of these moons – Anthe and Methone – are in mean-motion resonances with Saturn's moon Mimas. Specifically, they occupy the 10:11 and 14:15 corotation eccentricity resonances, respectively (Spitale et al., 2006; Cooper et al., 2008; Hedman et al., 2009). Both of these moons are also embedded in very faint, longitudinally-confined ring arcs (Roussos et al., 2008; Hedman et al., 2009). This material probably represents debris that was knocked off the relevant moons at low velocities and thus remains trapped in the same corotation resonance as its source body.

Images from Cassini also demonstrated that a similar arc of material exists within Saturn's G-ring, around 167,500 km from Saturn's center (Hedman et al., 2007). Images of this structure taken over the course of several years showed that it was also confined by a (7:6) corotation eccentricity resonance with Mimas. Furthermore, in situ measurements of the plasma environment in the vicinity of the arc suggested that it contains a significant amount of mass in particles larger than the dust-sized grains that are the dominant source of scattered light observed in images (Hedman et al., 2007).

In late 2008, during Cassini's Equinox Mission (2008–2010), images of the arc taken at lower phase angles and higher resolutions than previously possible revealed a small, discrete object. Since the object was most visible at low phase angles and could be tracked over a period of roughly 600 days, it is almost certainly not a transient clump of dust but instead a tiny moonlet that represents the largest of the source bodies populating the arc. The discovery of this object was therefore announced in an IAU circular, where it was designated S/2008 S1 (Porco et al., 2009). More recently the International Astronomical Union has given it the name Saturn LIII/Aegaeon. As will be shown below, Aegaeon, like Anthe and Methone, occupies a corotation eccentricity resonance with Mimas, and all three of these small moonlets are associated with arcs of debris. These three objects therefore represent a distinct class of satellites and comparisons among the ring–moon systems have the potential to illuminate the connection between moons and rings.

Section 2 below describes the currently available images of Aegaeon and how they are processed to obtain estimates of the brightness and position of this object. Section 3 presents a preliminary analysis of the photometric data, which indicate that this object is approximately 500 m in diameter. Section 4 describes

☆ This paper is dedicated to the memory of Kevin Beurle.

* Corresponding author.
E-mail address: mmhedman@astro.cornell.edu (M.M. Hedman).

0019-1035/$ - see front matter © 2009 Elsevier Inc. All rights reserved.
doi:10.1016/j.icarus.2009.10.024

the orbital solutions to the astrometric data, which demonstrate that Aegaeon's orbit is indeed perturbed by the 7:6 corotation eccentricity resonance with Mimas. However,we also find that a number of other resonances, including the 7:6 Inner Lindblad Resonance, strongly influence Aegaeon's orbital motion. Finally, Section 5 compares the various resonantly-confined moon/ring-arc systems to one another in order to clarify the relationship between Aegaeon and the G-ring.

2. Observational data

The images discussed here were obtained with the Narrow-Angle Camera (NAC) of the Imaging Science Subsystem (ISS) onboard the Cassini spacecraft (Porco et al., 2004). All images were initially processed using the CISSCAL calibration routines (Porco et al., 2004) that remove backgrounds, flat-field the images, and convert the raw data numbers into I/F, a standardized measure of reflectance. I is the intensity of the scattered radiation while πF is the solar flux at Saturn, so I/F is a unitless quantity that equals unity for a perfect Lambert surface viewed at normal incidence.

2.1. Image selection

The object was first noticed in two images taken on August 15 (DOY 228), 2008 (see Fig. 1). These images were part of a sequence designed to image the arc in the G-ring for the purposes of refining its orbit. Compared with previous imaging of the G-ring arc, the images used in this campaign were taken at lower phase angles and had better spatial resolution. This was more a result of the constraints imposed by the orbit geometry than a conscious effort to search for discrete objects in this region. When these images were taken, Cassini was in a highly inclined orbit with the ascending node near apoapse on the sunward side of the planet close to Titan's orbit. During these ringplane crossings, the faint rings could be imaged at high signal-to-noise, and the low-phase angles were considered desirable because this geometry was comparatively rarely observed prior to this time. However, this geometry also turned out to be useful for detecting small objects in the G-ring.

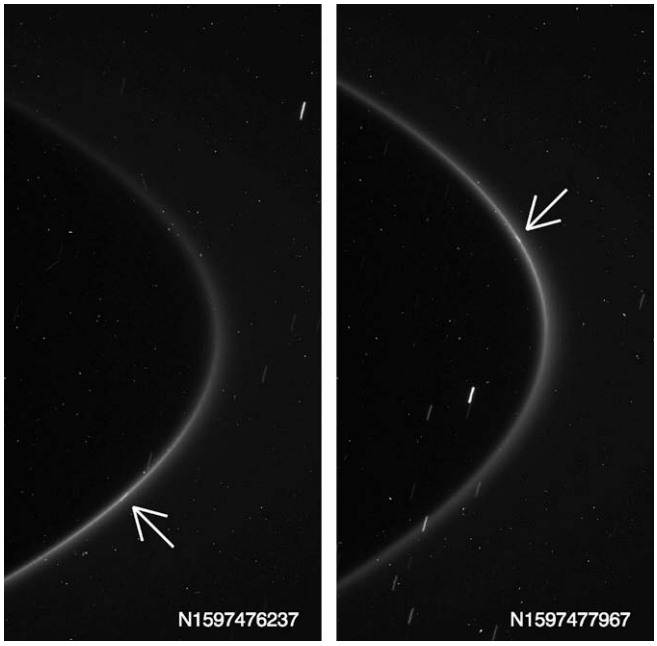

Fig. 1. The pair of images taken on August 15 (DOY 228), 2008 in which Aegaeon was first noticed. The arrows point to this object, which appears as a small streak within the core of the G-ring due to its orbital motion through the field of view over the course of these long-exposure images. Both images are rotated so that Saturn's north pole would point towards the top of the page.

Two images from this sequence (Fig. 1) contained the core of the arc and also showed a short, narrow streak in the G-ring. The streaks are aligned with the local orbital motion of the arc and are clearly not aligned with the streaks associated with stars in the field of view. The lengths of the streaks are consistent with the expected movement of an object embedded in the arc over the exposure time, and the positions of the streaks in the two images are consistent with such an object's motion over the ~30 min between the two images.

Since this sequence was part of a larger campaign designed to track the arc and refine its orbit, this object was quickly recovered in subsequent image sequences targeted at the arc with comparable viewing geometries, yielding 17 additional images of the object (Fig. 2). With these data, a preliminary orbit fit was used to search for earlier images of the object. However, only two images from the prime mission turned out to provide clear detections of Aegaeon (Fig. 3). This paucity of pre-discovery images is because this object is both extremely faint and embedded in the G-ring arc. While the object's faintness means that it cannot be clearly detected in images where the exposure times are too short, its proximity to the G-ring arc means that its signal cannot be isolated if the image resolution is too low or the phase angle is too high.

Table 1 lists the 21 NAC images used in this analysis, which are all the images prior to February 20 (DOY 051), 2009 in which Aegaeon has been securely identified. These images cover a time interval of almost 600 days and a range of phase angles from 13° to 43°.

2.2. Image data reduction

Since Aegaeon is not resolved in any of the images listed in Table 1, the only data we can extract from each image are its position in the field of view and its total integrated brightness. However, estimating even these parameters from these images is challenging because the light from Aegaeon is smeared out into a streak and because the light from the object must be isolated from the background signal from the G-ring arc. The following procedures were used to obtain the required photometric and astrometric data.

In order to isolate the moon's signal from that of the G-ring, each image was first roughly navigated based on stars within the field of view. Then, the radius and longitude in the ringplane observed by each pixel was computed. Based on visual inspection of the image, a region of the image containing the arc was selected (in general these regions are 10–20 pixels across). A second region extending 10 pixels beyond this zone on either side along the ring was then used to construct a radial profile of the G-ring and arc in the vicinity of the moon. A background based on this profile was then subtracted from the pixels in the selected region, which removes the signal from the G-ring and arc, leaving behind only the signal from Aegaeon itself.

Two images were handled slightly differently because they were taken in a nearly-edge-on viewing geometry (N1563866776 and N1603168767). In these cases instead of computing radius and longitude for each pixel, we compute the radius and vertical height above the ringplane and remove a vertical brightness profile from the region around the object.

After separating Aegaeon's signal from the G-ring, the total brightness of the object in each image is estimated in terms of an effective area, which is the equivalent area of material with $I/F = 1$ required to account for the observed brightness:

$$A_{eff} = \sum_x \sum_y I/F(x,y) * \Omega_{pixel} * R^2, \quad (1)$$

where x and y are the line and sample numbers of the pixels in the selected region, $I/F(x,y)$ is the (background-subtracted) brightness

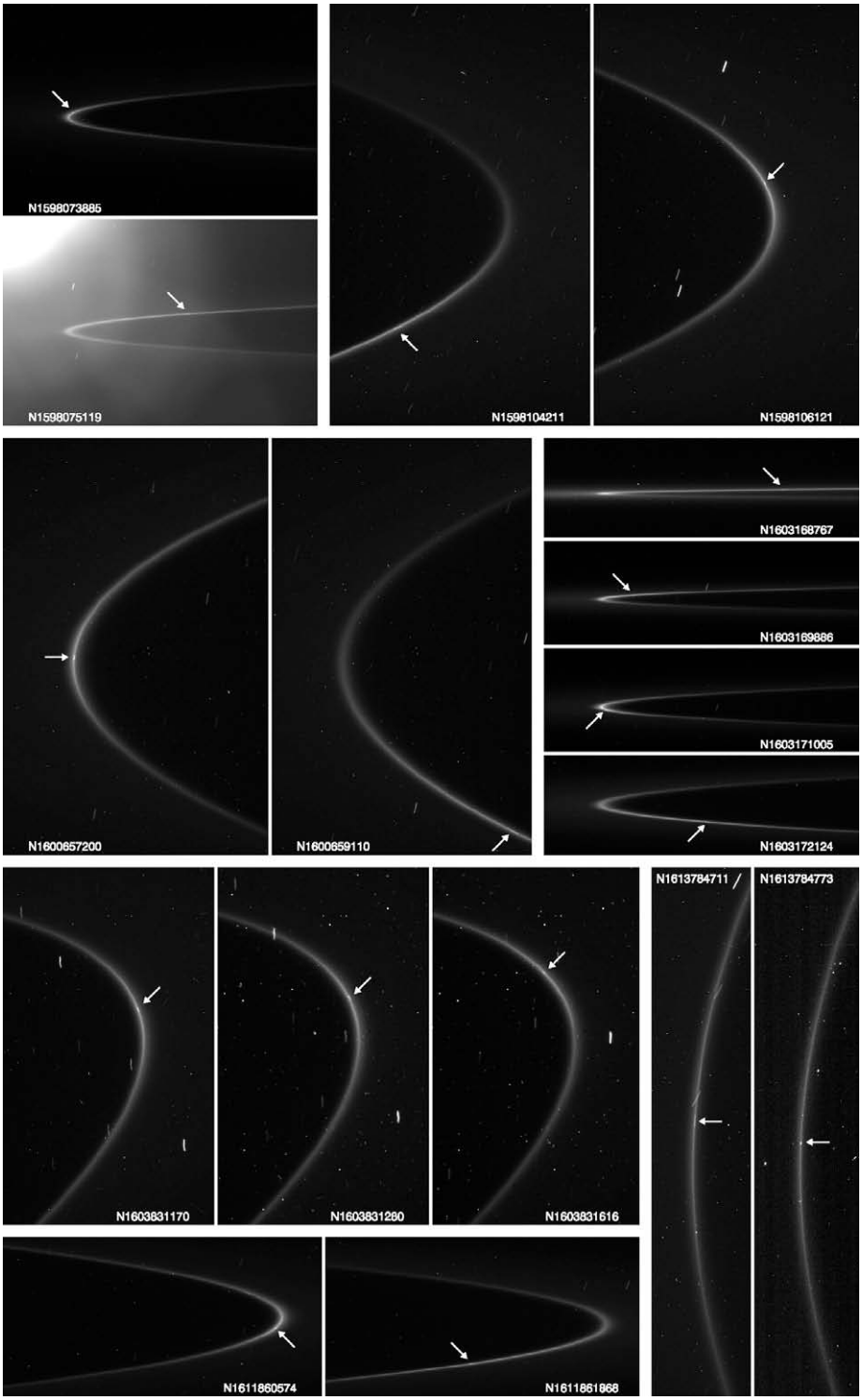

Fig. 2. Other low-phase, high-resolution images of Aegaeon obtained from late 2008 to February 20 (DOY 051), 2009. In each image the object's location is highlighted with an arrow. All images are rotated so Saturn's north pole would point upwards. Note the bright feature in the upper left corner of image N1598075119 is due to Tethys being in the camera's field of view.

of the streak in the x,y pixel, $\Omega_{pixel} = (6\ \mu\text{rad})^2$ is the assumed solid angle subtended by a NAC pixel, and R is the distance between the spacecraft and the object during the observation. The assumed values for R (given in Table 1) are based on the best current orbital solution (see below).

Similarly, the object's mean position in the field of view was determined by computing the coordinates (in pixels) of the streak's center of light x_c and y_c:

$$x_c = \frac{\sum_x \sum_y x * I/F(x,y)}{\sum_x \sum_y I/F(x,y)}, \tag{2}$$

$$y_c = \frac{\sum_x \sum_y y * I/F(x,y)}{\sum_x \sum_y I/F(x,y)}. \tag{3}$$

For purposes of deriving the object's orbit, these estimates of Aegaeon's position within the camera's field of view are converted into estimates of its right ascension and declination on the sky as seen

Table 1
Images of Aegaeon.

Image	Midtime (SCET)[a]	Range (km)	Phase (deg.)	B[b] (deg.)	A_{eff}[c] (km^2)	Line[d]	Sample[d]	RA[e] (deg.)	DEC.[e] (deg.)
N1560588018	2007-166T08:05:49.180	1708692	42.9	+0.46	0.045	521.5	396.3	191.35064	+5.1764862
N1563866776	2007-204T06:51:37.403	1432779	14.5	+0.01	0.038	500.4	523.1	60.26121	+3.2032395
N1597476237	2008-228T06:45:07.972	1188766	28.2	+4.89	0.074	150.7	232.0	138.26865	−4.1721804
N1597477967	2008-228T07:13:57.959	1215278	28.2	+5.14	0.072	227.9	555.0	138.32963	−4.3106590
N1598073885	2008-235T04:46:01.799	1171032	12.9	−0.75	0.072	533.4	593.5	151.92415	+3.1237490
N1598075119	2008-235T05:06:35.775	1154016	13.0	−0.56	0.097	745.8	619.6	151.93067	+2.7766773
N1598104211	2008-235T13:11:17.572	1179499	28.4	+3.75	0.062	138.0	244.5	137.76804	−3.0640496
N1598106121	2008-235T13:43:07.559	1209028	28.4	+4.02	0.074	321.2	512.2	137.80784	−3.2486713
N1600657200	2008-265T02:20:48.735	1205305	15.2	+4.34	0.079	659.9	377.9	153.49124	−1.8808037
N1600659110	2008-265T02:52:38.706	1177863	15.5	+4.62	0.082	977.0	56.1	153.49796	−2.2741652
N1603168767	2008-294T04:00:07.953	1203664	15.0	+0.09	0.082	856.5	522.8	151.72360	+2.2458309
N1603169886	2008-294T04:18:46.945	1188111	14.9	+0.26	0.105	576.5	525.5	151.87725	+2.0895161
N1603171005	2008-294T04:37:25.937	1172420	14.9	+0.43	0.081	526.5	513.0	151.95312	+1.9205764
N1603172124	2008-294T04:56:04.929	1156757	14.9	+0.60	0.077	713.8	493.2	151.94754	+1.7380537
N1603831170	2008-301T19:59:56.266	1197708	30.6	+4.81	0.077	254.7	414.0	137.60681	−4.0823444
N1603831280	2008-301T20:01:46.273	1199390	30.6	+4.82	0.101[f]	123.4	217.6	137.61323	−4.0912850
N1603831616	2008-301T20:07:22.279	1204524	30.6	+4.87	0.094[f]	104.9	241.5	137.63718	−4.1180591
N1611860574	2009-028T18:22:32.246	1180159	35.0	−1.49	0.072	510.1	500.8	133.96654	+1.8936283
N1611861868	2009-028T18:44:06.221	1199209	34.8	−1.22	0.059	273.8	403.9	134.17857	+1.6322662
N1613784711	2009-051T00:51:05.547	1186785	20.5	+13.6	0.070	291.2	516.0	158.59803	−10.684674
N1613784773	2009-051T00:52:28.255	1185601	20.6	+13.6	0.063	289.0	475.1	158.61153	−10.715706

[a] Spacecraft event time.
[b] Ring opening angle.
[c] Effective area of the object (see text).
[d] The origin of the image *line* and *sample* coordinate system is at the center of the top left pixel, with *line* increasing downwards and *sample* to the right, when the image is displayed in its normal orientation. The spacecraft $-x$-axis points in the direction of increasing *line* and $-z$-axis in the increasing *sample* direction. Estimated measurement uncertainties ~0.5 pixel in line and sample.
[e] RA and DEC refer to right ascension and declination in the International Celestial Reference Frame (ICRF).
[f] Images N1603831280 and N1603831616 taken through RED and IR1 filters, respectively. All other images taken through clear filters.

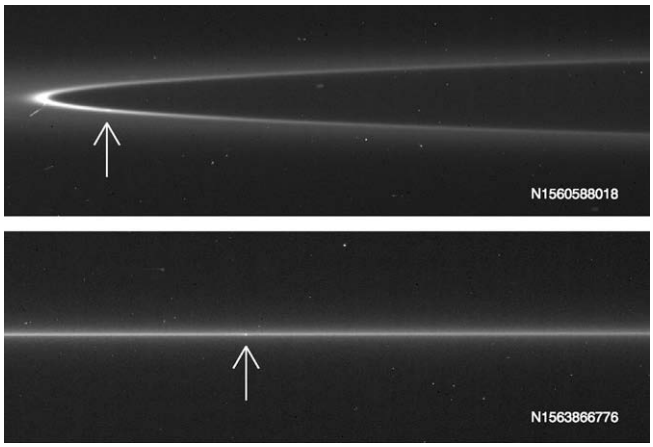

Fig. 3. The only two clear images of Aegaeon obtained prior to mid-2008 found to date. In each image the location of the object is highlighted with an arrow. Both images are rotated so Saturn's north pole would point roughly up.

by Cassini. This is accomplished by comparing the center-of-light coordinates of Aegaeon to the center-of-light coordinates of various stars in the field of view.

Table 1 lists all derived parameters for each of the relevant images.

3. Photometric analysis and the size of Aegaeon

Table 1 includes 19 measurements of Aegaeon's brightness through the NAC's clear filters over a range of phase angles between 13° and 43°.[1] In the absence of disk-resolved images of this object, these photometric data provide the only basis for estimating its size.

For the above range of phase angles α, the effective area A_{eff} of a spherical object is usually well approximated by the following form:

$$A_{eff} = p_{eff} A_{phys} 10^{-\beta\alpha/2.5}, \quad (4)$$

where A_{phys} is the physical cross-sectional area of the object, p_{eff} is the effective geometric albedo (neglecting the opposition surge) and β is the linear phase coefficient (Veverka, 1977). Even if the object is not spherical, we still expect that $\langle A_{eff}(\alpha)\rangle$ – the effective area at a given phase angle averaged over object orientations – will have the same basic form:

$$\langle A_{eff}\rangle = p_{eff}\langle A_{phys}\rangle 10^{-\beta\alpha/2.5}, \quad (5)$$

where $\langle A_{phys}\rangle$ is the average physical cross-section of the object.

Fitting the photometric data over a sufficiently broad range of phase angles to Eq. (5) can provide estimates of the linear phase coefficient β and the product $p_{eff}\langle A_{phys}\rangle$. However, to convert the latter into an estimate of the object's size requires additional information about p_{eff}, which can be obtained from comparisons with similar objects. For Aegaeon, the best points of comparison are Pallene, Methone and Anthe, three small saturnian moons whose orbits lie between those of Mimas and Enceladus. These moons are the closest in size to Aegaeon and are in similar environments (Pallene, Methone, Anthe and Aegaeon are all embedded in faint rings or arcs of material).

To quantitatively compare the photometric characteristics of these various moons, we computed the effective areas A_{eff} of Pallene, Methone and Anthe from a series of images taken over a similar range of phase angles as the Aegaeon images. Tables 2–4 list the images of Pallene, Methone, and Anthe used in this analysis. Since the goal here is to make comparisons between different moons and not to do a complete photometric analysis of these objects, the images used in the current study are only

[1] Two images (N1603831280 and N1603831616) were obtained using the RED (λ_{eff} = 649 nm) and IR1 (λ_{eff} = 751 nm) filters, respectively. While Aegaeon's brightness is the same at both these wavelengths at the 5% level, it is premature to make any definite conclusions about Aegaeon's color based on such limited data.

Table 2
Images of Pallene.

Image name	Range (km)	Phase (deg.)
N1495207156	1140706	36.9
N1495207303	1141683	36.9
N1506004385	1619552	44.5
N1506004655	1616699	44.4
N1507534034	1396476	48.9
N1555052913	1703818	39.0
N1575630032	1564127	16.9
N1575675932	1878085	15.5
N1577009966	1748173	19.0
N1580356385	1362288	20.4
N1580527536	1515543	24.8
N1581771720	1982140	30.8
N1583629498	1466714	36.8
N1584374373	1732141	19.9
N1585394936	1436059	35.9
N1585439051	1435253	38.5
N1586003505	1074505	13.7
N1586193031	1428772	32.7
N1587716367	1226979	24.4
N1587848623	1649791	28.8
N1589547370	1391832	33.2
N1591878927	1024706	10.2
N1595480632	806986	25.2
N1595509222	1186319	30.0
N1597581787	999582	35.3
N1598065360	978305	16.7
N1599452540	1100556	22.2
N1599960489	950479	18.9
N1602671923	1049439	37.1

Table 3
Images of Methone.

Image name	Range (km)	Phase (deg.)
N1495209176	1254846	20.1
N1495209323	1252910	20.0
N1506063845	995105	46.7
N1559173514	1701162	42.3
N1563933254	1870692	12.2
N1575055798	1837767	45.6
N1575629432	1824208	14.1
N1579322353	1297453	11.2
N1579399258	1667738	16.5
N1579447529	1545970	21.5
N1580484276	1466609	21.8
N1580614807	1983810	26.2
N1581772425	1774910	37.2
N1582719892	1717981	35.3
N1583323256	1377304	10.5
N1583323886	1373418	10.4
N1583324096	1372066	10.4
N1583344421	1179950	12.4
N1583757119	1646695	41.8
N1584374043	1651275	20.6
N1584714966	1559604	44.5
N1585394126	1577946	32.3
N1585438211	1363938	41.5
N1586002605	1389381	21.0
N1587747477	1539000	24.0
N1588451222	1361525	19.3
N1588781885	1329843	43.1
N1590864949	992002	38.6
N1591525464	1113846	35.2
N1591762166	945278	31.7
N1591878207	1211541	9.3
N1595481232	832264	26.4
N1595510182	1239193	26.8
N1596877322	1037741	25.9
N1597581487	1026605	35.1
N1598065750	1286329	13.5
N1599961704	1318799	26.9
N1600651648	1289847	29.5
N1600751290	1357620	28.2
N1601291954	1344186	16.2
N1601855958	994265	31.2
N1602578562	1370014	27.4
N1603214386	1309285	16.7
N1604534936	1226594	21.5
N1604570261	1281208	33.8

a selected subset of NAC clear-filter images that were expected to give the most reliable brightness data based on the spacecraft range and exposure duration. All these images were taken from within about 2 million kilometers of the target moon and had exposure durations that were long enough for the moon's signal to be measured accurately but short enough that there was no chance of saturation.

For each image, we computed the total integrated brightness in a 14-by-14 pixel wide zone containing the moon above the average background level in a 5-pixel wide annulus surrounding the selected region. These total brightness measurements were then converted into effective areas using the range between the spacecraft and the moon as described in Eq. (1).

Fig. 4 shows the resulting estimates of A_{eff} as a function of phase angle for Pallene, Methone, Anthe and Aegaeon. The data for Pallene, Methone and Anthe all show significant scatter around the main trends. In all three cases, this scatter can be attributed to variations in the orientation of a non-uniform or non-spherical object relative to the spacecraft. (As will be discussed in a future work, all three moons appear to have significant ellipticities with the long axis pointing towards Saturn.) The Aegaeon data are divided into two groups in this plot based on whether the observation had a ring opening angle $|B|$ greater or less than 1°. Because the contrast of the moon against the background G-ring is reduced at lower ring opening angles due to the increased surface brightness of the ring material, the $|B| > 1^\circ$ data are considered to be more reliable measurements of A_{eff}.

Despite the scatter, it is clear that the data from all four objects can be fit to a mean trend of the form given in Eq. (5). The lines in the plots show the resulting best-fit trend, while Table 5 gives the resulting fit parameters (note only the $|B| > 1^\circ$ data are used for the Aegaeon fit). Because the scatter in the data points from each moon is not random error, but instead systematic variations associated with viewing geometry, error bars on these parameters are not reported here.

The phase coefficients of Anthe, Pallene and Methone are reasonable values for small airless objects (compare with values for asteroids in Bowell and Lumme (1979)), while the coefficient for Aegaeon is somewhat on the low side, which may be because a residual unsubtracted G-ring signal adds a slightly forward-scattering component to its phase curve. Alternatively, Aegaeon may have a smoother surface than the other moons (Veverka, 1971).

Of all of these moons, only Pallene has been observed with sufficient resolution to obtain a well-defined mean radius of 2.2. ± 0.3 km (Porco et al., 2007). Given the observed value of $p_{eff}\langle A_{phys}\rangle = 7.38\ \mathrm{km}^2$, this would imply that $p_{eff} = 0.49$ for this moon. Assuming that all four objects have roughly the same geometric albedo, we obtain estimates of the mean radii of Methone and Anthe of 1.6 km and 1.1 km, respectively. The estimated size of Methone matches the estimate derived from crudely resolved images (1.6 ± 0.6 km, Porco et al., 2007), and the radius of Anthe matches previous estimates based on its brightness relative to Pallene (Cooper et al., 2008). Applying this same albedo to Aegaeon suggests a radius of 240 m. Assuming geometric albedos between 0.1 and 1.0 gives a range of radii between 160 and 520 m, so although the size of the object is still uncertain, it is almost certainly less than 1 km across.

Table 4
Images of Anthe.

Image name	Range (km)	Phase (deg.)
N1572352978	2304579	22.6
N1572353038	2303910	22.6
N1572353098	2303241	22.6
N1572353158	2302571	22.6
N1572353218	2301901	22.6
N1572353442	2299328	22.7
N1575629162	1802824	14.3
N1579321873	1440693	11.3
N1579364158	1258476	17.9
N1580356175	1214702	20.0
N1581514393	1472750	21.2
N1582636683	1783724	27.7
N1582768099	1419578	41.9
N1583627560	1746544	33.9
N1585394528	1619129	31.4
N1586002250	1235543	23.5
N1586004500	1271592	23.4
N1591878477	1065302	9.7
N1596338308	1242828	28.9
N1596721036	861867	21.8
N1598065060	990740	17.2
N1599961164	1029567	30.0
N1600583458	965664	28.8
N1600749010	1034862	27.2
N1601479534	854848	48.2
N1601778096	1097628	34.8
N1601856348	1202995	32.6
N1602516863	1273685	15.0
N1602577242	1331594	29.3
N1603720951	935528	36.3
N1603880961	1059788	22.0
N1604739758	1061249	44.8

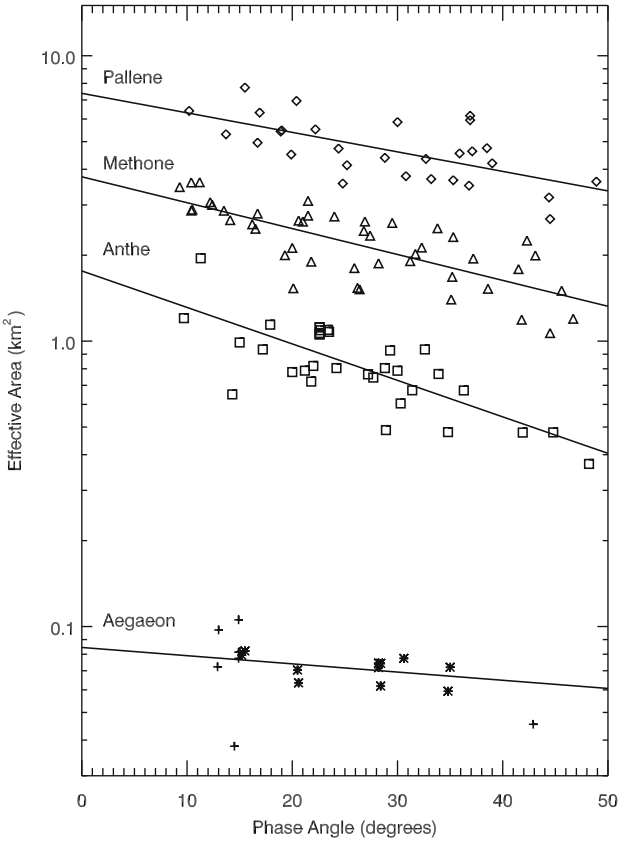

Fig. 4. The effective areas of Pallene, Methone, Anthe and Aegaeon as functions of phase angle. Note that most of the scatter in the Pallene, Methone and Anthe around the trend-line are due to variations in the orientation of the moon relative to the spacecraft. Two subsets of the Aegaeon data are highlighted. The stars are data from images with ring opening angles above 1°, which are considered more reliable than those obtained at lower ring opening angles (marked as plusses) where the contrast of the object against the ring is weaker. Since the scatter in the data for each moon is dominated by systematic effects, statistical error bars are not included in this plot.

4. Orbital solutions

The methodology used to derive the orbital solution for Aegaeon follows the same basic procedures used by Cooper et al. (2008) with Anthe and Murray et al. (2005) with Polydeuces. As in those works, the solution is computed in a planetocentric reference frame where the x-axis corresponds to the direction of the ascending node of Saturn's equatorial plane on the equator of the International Celestial Reference Frame (ICRF); the z-axis is directed along Saturn's spin axis at epoch (pointing north); and the y-axis is orthogonal to x and z and oriented as required to produce a right-handed coordinate system. The chosen epoch for the orbital solution is 2008-228T06:45:07.972 UTC (the time of the first discovery image). The assumed values for Saturn's pole position and gravitational field are given in Table 6, while Table 7 lists the SPICE kernels (Acton, 1996) used in the orbit determination and numerical modeling.

As with Anthe and other small saturnian satellites, the orbit of Aegaeon cannot be accurately fit with a simple precessing elliptical model (see below). Thus the data were fit to a numerical integration of the full equations of motion in three dimensions, solving for the initial state of Aegaeon at epoch. This model included perturbations from the Sun, Saturn, Jupiter, the eight major satellites of Saturn (Mimas, Enceladus, Tethys, Dione, Rhea, Titan, Hyperion and Iapetus), as well as the smaller moons Prometheus, Pandora, Janus and Epimetheus. The forces from these perturbers were calculated using position vectors extracted from the JPL ephemerides listed in Table 7. These position vectors were rotated from the ICRF to the saturn-centric reference frame using the pole position given in Table 6, obtained by precessing the pole position of Jacobson (2004) to the chosen epoch, using rates of −0.04229 deg./cy in right ascension and −0.00444 deg./cy in declination (Jacobson, 2004). Terms up to J_6 in Saturn's gravitational field were taken into

Table 5
Summary of photometric properties of the small moons.

Moon	β (mag/deg.)	$p_{eff}\langle A_{phys}\rangle$ (km^2)	$\langle r_{phys}\rangle$[a] (km)
Pallene	0.017	7.38	2.2
Methone	0.023	3.76	1.6
Anthe	0.032	1.76	1.1
Aegaeon[b]	0.007 mag/deg.	0.084	0.24

[a] Assuming all four moons have $p_{eff} = 0.49$ (required to match mean radius of Pallene).
[b] Fit to only the $|B| > 1°$ data.

Table 6
Saturn constants used in orbit fitting and numerical modeling.

Constant	Value[a]	Units
Pole (RA, DEC)	40.5837626692582, 83.5368877051669	deg.
GM	37931207.1585	km^3 s^{-2}
Radius, R_s	60330	km
J_2	0.016290543820	
J_4	−0.000936700366	
J_6	0.000086623065	

[a] Pole position from SPICE kernel cpck19Sep2007.tpc, precessed to the fit epoch. Reference radius from Kliore et al. (1980). Zonal harmonics and GM from cpck19Sep2007.tpc.

Table 7
SPICE kernels used in orbit fitting and numerical modeling.

Kernel name[a]
pck00007.tpc
naif0009.tls
cas00130.tsc
cpck19Sep2007.tpc
cpck_rock_01Oct2007_merged.tpc
de414.bsp
jup263.bsp
sat286.bsp
080806AP_SCPSE_08138_10182.bsp
081211AP_SCPSE_08346_08364.bsp
090120AP_SCPSE_09020_09043.bsp
090202BP_SCPSE_09033_09044.bsp
090209AP_SCPSE_09037_09090.bsp
090305AP_SCPSE_09064_09090.bsp
081125AP_RE_90165_18018.bsp
070416BP_IRRE_00256_14363.bsp
070727R_SCPSE_07155_07170.bsp
070822R_SCPSE_07170_07191.bsp
071017R_SCPSE_07191_07221.bsp
071127R_SCPSE_07221_07262.bsp
080117R_SCPSE_07262_07309.bsp
080123R_SCPSE_07309_07329.bsp
080225R_SCPSE_07329_07345.bsp
080307R_SCPSE_07345_07365.bsp
080327R_SCPSE_07365_08045.bsp
080428R_SCPSE_08045_08067.bsp
080515R_SCPSE_08067_08078.bsp
080605R_SCPSE_08078_08126.bsp
080618R_SCPSE_08126_08141.bsp
080819R_SCPSE_08141_08206.bsp
080916R_SCPSE_08206_08220.bsp
081031R_SCPSE_08220_08272.bsp
081126R_SCPSE_08272_08294.bsp
081217R_SCPSE_08294_08319.bsp
090120R_SCPSE_08319_08334.bsp
090202R_SCPSE_08334_08350.bsp
090225R_SCPSE_08350_09028.bsp
090423R_SCPSE_09028_09075.bsp

[a] Kernels are available by anonymous ftp from ftp://naif.jpl.nasa.gov/pub/naif/CASSINI/kernels.

Table 8
GM values for other perturbing bodies used in orbit fitting and numerical modeling.

Body	GM[a] ($km^3\ s^{-2}$)
Sun	132712440044.2083
Jovian system	126712764.8582231
Prometheus	0.01058
Pandora	0.00933
Janus	0.12671
Epimetheus	0.03516
Mimas	2.50400409891677
Enceladus	7.20853820010930
Tethys	41.2103149758596
Dione	73.1128918960295
Rhea	153.941891174579
Titan	8978.13867043253
Hyperion	0.370566623898283
Iapetus	120.504895547942

[a] Values from SPICE kernels cpck19Sep2007.tpc and cpck_rock_10Oct2007_merged.tpc.

account. The adopted *GM* values for the satellites, etc. are given in Table 8.

Numerical integration of both the equations of motion and the variational equations was performed using the 12th-order Runge–Kutta–Nyström RKN12(10)17M algorithm of Brankin et al. (1989). For more details on the fitting procedures, see Murray et al. (2005). The final solution for the state vector at epoch in the planetocentric frame, from a fit to the full time-span of observations, is given in Table 9. All the observations listed in Table 1 were included in this fit with equal weights. Fig. 5 shows the orbital coverage of the available observations, based on the numerically integrated positions. Note the data fall in two clusters, which correspond to the two ansae of the orbit when the rings are viewed at low phase angles during the observation epoch.

Table 9
Solution for the planetocentric state vector of Aegaeon, from a fit to *Cassini* ISS data in the ICRF. Epoch is 2008-228T06:45:07.972 UTC (2008-228T06:46:13.154 or JD 2454693.78209670 TDB).

Aegaeon		Units
x	0.123456139640300E+06 ± 3.2855191576	km
y	0.111538222264526E+06 ± 2.4140374161	km
z	−0.188394292598307E+05 ± 1.2178065755	km
$\dot{x}$	−0.101036088689253E+02 ± 0.0003052052	km s^{-1}
$\dot{y}$	0.111912435677253E+02 ± 0.0001445381	km s^{-1}
$\dot{z}$	0.447482819944934E−01 ± 0.0001146560	km s^{-1}
rms	0.468	pixel
rms	0.578	arcsec

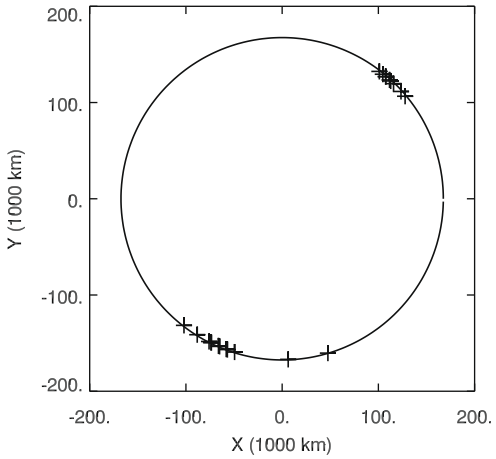

Fig. 5. Observational coverage of Aegaeon projected onto the equatorial plane of Saturn, with superimposed circle of radius 167,490 km.

Fit residuals are displayed as a function of time in Fig. 6. The overall rms fit residual is 0.468 pixels for the 21 NAC images, which is equivalent to 0.578 arcsec. This is comparable to the residuals for the NAC observations of Anthe (Cooper et al., 2008), which is remarkable given that in most of the images used here Aegaeon forms a streak several pixels long. This suggests that our methods for deriving the position of the moon are accurate, and that the systematic errors in the modeled orbit are small. The final rms uncertainty in the fitted position vector in the frame of integration is 4.3 km.

Table 10 lists the planetocentric orbital elements derived by fitting a uniformly precessing ellipse to the numerically integrated orbit of Aegaeon over a 1-day time-span, using a fine grid of regularly-spaced position vectors. These parameters include the semi-major axis a_{calc}, eccentricity e, inclination i, longitude of ascending node Ω, longitude of pericenter ϖ, longitude at epoch λ_o and mean motion n. Note that the calculated semi-major axis a_{calc} was obtained by first fitting for n and then converting to semi-major axis using the standard equations involving Saturn's gravitational harmonics (Nicholson and Porco, 1988). The apsidal and nodal rates were calculated using the expressions in Cooper and Murray (2004), incorporating terms up to J_6. It should be emphasized that the fitted elements in Table 10 represent only a snapshot of the orbit at the time epoch of fit (2008-001T12:00:00 UTC, chosen to be a

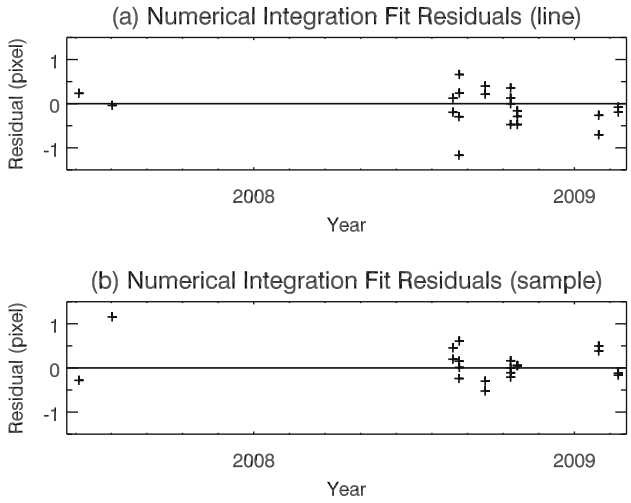

Fig. 6. Numerical-integration fit residuals in pixel units: (a) line and (b) sample.

time when Aegaeon was near the center of its librations, see below). In reality, the orbital elements show significant periodic variations due to resonant perturbations from Mimas, so a uniformly precessing ellipse will provide a poor approximation of the orbit over a time-span of more than a few days.

Fig. 7 shows the variations in the geometrical orbital elements over a period of 10 years. These plots were generated by integrating the initial state vector from Table 9, and state vectors were generated at 0.15-day intervals and converted into geometric orbital elements using standard methods (Borderies and Longaretti, 1994; Renner, 2004; Renner and Sicardy, 2006). Unlike conventional osculating elements, these geometric elements are not contaminated by short-period terms caused by planetary oblateness. There are clear periodic variations in all the orbital elements. The semi-major axis varies by ±4 km around a mean value of 167,494 km. The eccentricity ranges between nearly zero and 0.00047, and the inclination ranges from 0.0001° to 0.0019°. The mean values of a, e and i and the amplitude of their periodic variations are also given in Table 10. Note that when the eccentricity and inclination both periodically approach zero, the longitudes of node and pericenter change rapidly.

Since the G-ring arc appears to be confined by the 7:6 corotation eccentricity resonance with Mimas (Hedman et al., 2007), we expected that Aegaeon would also be trapped in this resonance. Figs. 8a and b show the time evolution of the resonant argument for the 7:6 corotation eccentricity resonance

$$\varphi_{CER} = 7\lambda_{Mimas} - 6\lambda_{Aegaeon} - \varpi_{Mimas}. \quad (6)$$

These data indicate that the argument librates, confirming that Aegaeon indeed occupies the 7:6 corotation eccentricity resonance with Mimas. This analysis also demonstrates that the dominant libration period is 1264 ± 1 days, consistent with the estimated libration periods of particles in the G-ring (Hedman et al., 2007).

The amplitude of the librations in this resonant argument is only ∼10°, so one might expect that Aegaeon's longitude would only deviate by a few degrees from its expected value assuming a constant mean motion. In reality, Aegaeon's longitude can drift by tens of degrees from its expected position assuming a constant mean motion (Fig. 9). These long-period drifts have a characteristic period of 70 years, comparable to the 70.56 year libration in Mimas' longitude caused by its resonance with Tethys (Vienne and Duriez, 1995). These variations therefore likely arise because the longitude of Mimas is itself perturbed by a resonance with Tethys. Note that over the course of the Cassini Mission, the residual longitude of Aegaeon has drifted backwards at a rate of approximately 0.01 deg./day. This probably explains why the best-fit mean-motion of the arc from the Cassini data was 445.475 ± 0.007 deg./day instead of the expected value of 445.484 deg./day (Hedman et al., 2007).

The corotation eccentricity resonance should primarily affect Aegaeon's orbital mean motion and computed semi-major axis, and have little effect on its eccentricity and inclination. However, there are clearly large fractional variations in both Aegaeon's eccentricity and inclination. Furthermore, these variations seem to be coupled, such that the eccentricity and inclination rise and fall together. This strongly suggests that additional resonances are influencing Aegaeon's orbit. In particular, the correlation be-

Table 10
Planetocentric orbital elements.

Parameter[a]	Fitted value	Units
Fit epoch	2008-001T12:00:00.000 UTC	UTC
	2008-001T12:01:05.183 TDB	TDB
	JD 2454467.00075444 TDB	TDB
Semi-major axis, a_{calc}	167493.665 ± 0.004	km
Eccentricity, e	0.00042277 ± 0.00000004	
Inclination, i	0.0007 ± 0.6	deg.
Longitude of ascending node, Ω	30 ± 298	deg.
Longitude of pericenter, ϖ	352.694 ± 0.005	deg.
Mean longitude, λ	45.606789 ± 0.000004	deg.
Mean motion, n	445.48328 ± 0.00002	deg./day
Pericenter rate, $\dot{\varpi}_{calc}$	1.43691010	deg./day
Nodal rate, $\dot{\Omega}_{calc}$	−1.43229434	deg./day
Parameter	Mean value ± libration	Units
Semi-major axis, a_{mean}	167494 ± 4	km
Eccentricity, e_{mean}	0.00024 ± 0.00023	
Inclination, i_{mean}	0.0010 ± 0.0009	deg.
Resonant argument (CER)	$7\lambda_{Mimas} - 6\lambda_{Aegaeon} - \varpi_{Mimas}$	
Resonant argument's libration period (CER)	1264 ± 1	days
Resonant argument (ILR)	$7\lambda_{Mimas} - 6\lambda_{Aegaeon} - \varpi_{Aegaeon}$	
Resonant argument's libration period (ILR)	824 ± 1	days

[a] All longitudes measured directly from ascending node of Saturn's equator on the ICRF equator. Inclination measured relative to Saturn's equatorial plane. Quoted uncertainties in the upper half of the table are the formal 1σ values from the fit. Note the values in the upper half of the table are values at a particular point in time and are provided as a guide. They are not suitable as starting conditions in integrations for the equation of motion. Mean values and their librations in the lower half of the table were obtained from a numerical integration of the period 2004-001 to 2014-001, taking into account the resonant behavior.

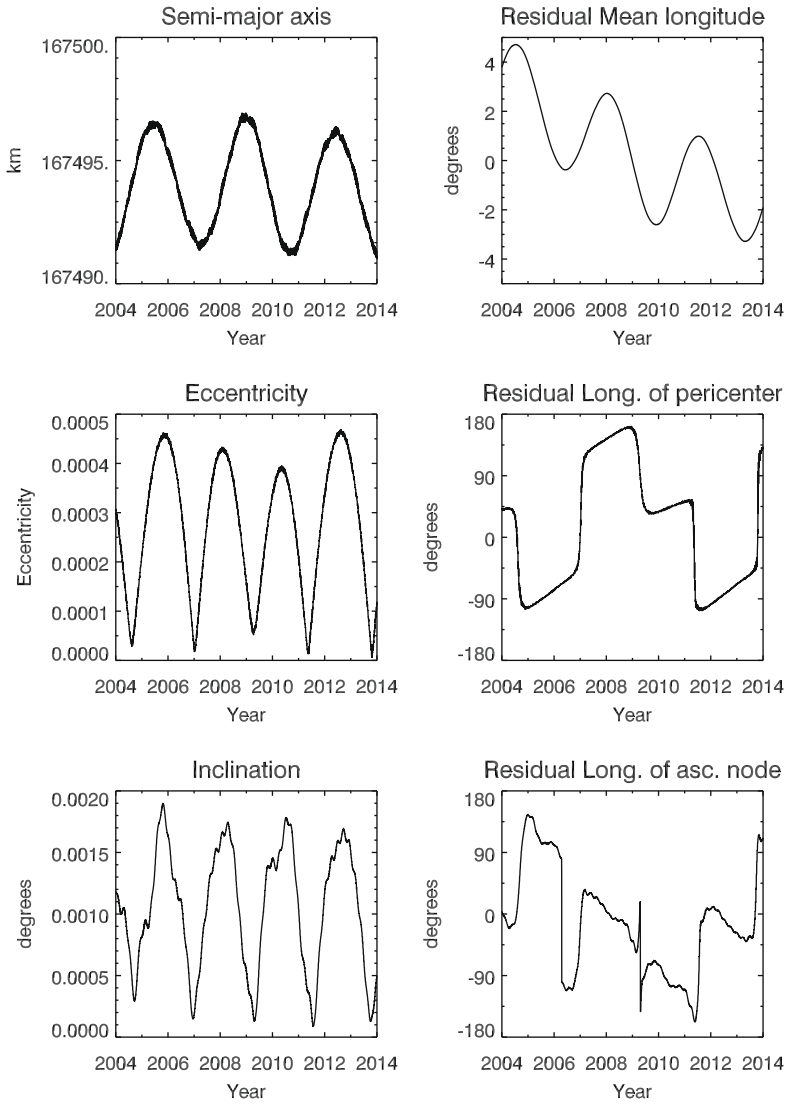

Fig. 7. Geometric orbital elements between 2004 and 2014 derived from the numerical integration, including perturbations from the eight major satellites of Saturn plus Prometheus, Pandora, Janus and Epimetheus. Linear background trends have been subtracted from the mean longitude, pericenters and nodes prior to plotting (the rates being 445.482 deg./day, 1.146 deg./day and −1.098 deg./day, respectively).

tween the moon's eccentricity and inclination suggests a Kozai-like mechanism may be involved. However, unlike a classical Kozai Resonance (Kozai, 1962) where the correlation between the eccentricity and inclination is negative, in this case the correlation between these two parameters is positive.

To further explore these aspects of Aegaeon's orbital evolution, we looked at the time evolution of the fourteen valid resonant arguments to fourth degree in the eccentricities and the inclinations of the form $\varphi = 7\lambda_{Mimas} - 6\lambda_{Aegaeon} + \cdots$. In addition to the corotation eccentricity resonance, we found 7 other resonant arguments that exhibited interesting behavior; they are listed in Table 11. These include the resonant argument of the 7:6 Inner Lindblad Resonance φ_{ILR}, two resonant arguments φ_x and φ_y that can be written as linear combinations of φ_{CER} and φ_{ILR}, and four resonant arguments involving the nodes of Mimas and Aegaeon ($\varphi_a - \varphi_d$). Integrations of a few test cases where the initial state vector was shifted within the error bars showed the same fundamental behavior. While a detailed investigation of all of these resonant terms is beyond the scope of this paper, we will briefly discuss the behavior of a few of these resonant arguments.

Fig. 8c and d shows the time evolution of the resonant argument of the Inner Lindblad Resonance $\varphi_{ILR} = 7\lambda_{Mimias} - 6\lambda_{Aegaeon} - \varpi_{Aegaeon}$. This resonant argument appears to spend most of its time librating within ±90° of zero with a period of 824 ± 1 days, interspersed with brief episodes where the resonant argument circulates around 360°. The dominant libration period of this argument equals the synodic period of the difference between Aegaeon's and Mimas' pericenters, which is reasonable since $\varphi_{ILR} = \varphi_{CER} + \varpi_{Mimas} - \varpi_{Aegaeon}$. The alternations between libration and circulation imply that Aegaeon's orbit lies at the boundary of the ILR, and its free eccentricity is almost equal to the forced eccentricity from the Lindblad Resonance. As noted previously, the total eccentricity periodically approaches zero and the pericenter longitude changes rapidly, as seen in Fig. 7. During these episodes, φ_{ILR} could either librate through zero or circulate through 180° depending on whether the forced eccentricity (which will vary with time as Aegaeon's orbit librates around the corotation eccentricity resonance) is slightly larger or smaller than the free eccentricity.

By way of comparison, it is interesting to note that Saturn's small moon Methone also appears to occupy both a corotation eccentricity resonance and an Inner Lindblad Resonance with Mimas (Spitale et al., 2006; Hedman et al., 2009). However, the 14:15 resonances occupied by Methone are separated by less than 4 km in semi-major axis, while the 7:6 resonances affecting Aegaeon's orbit are

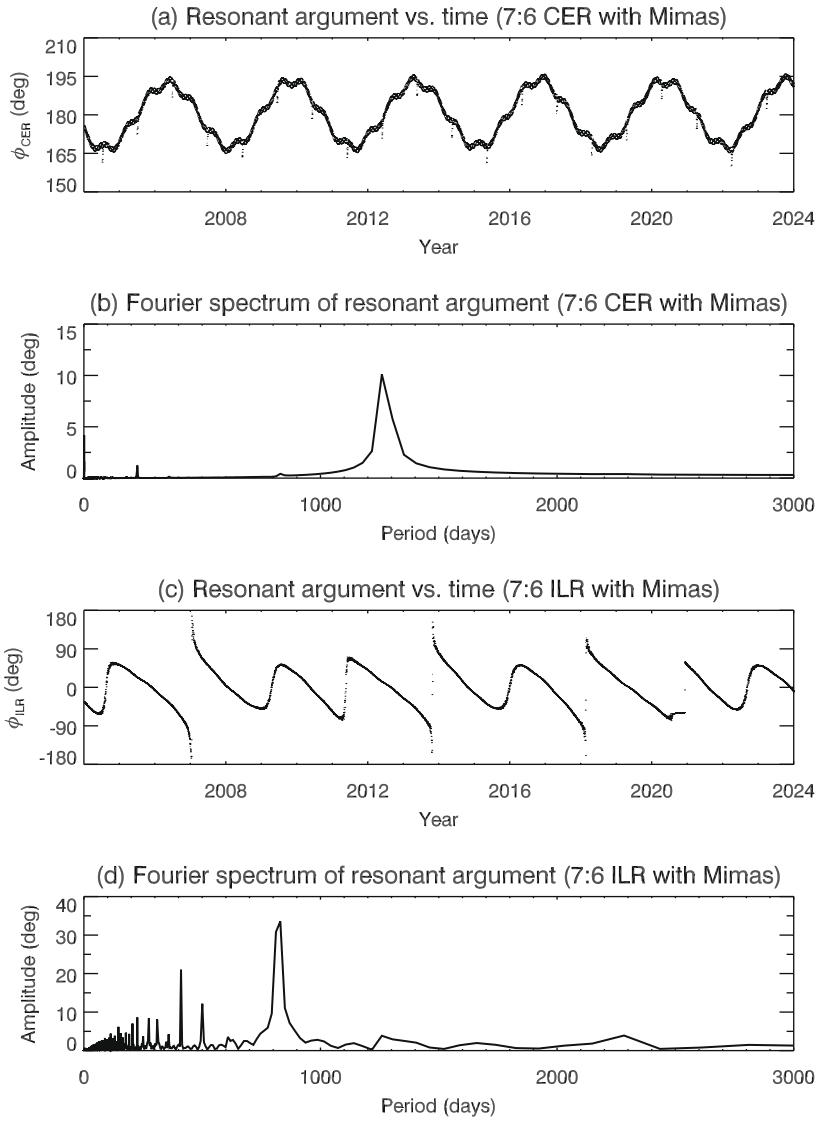

Fig. 8. (a) Resonant argument of the 7:6 CER ($\varphi = 7\lambda_{Mimas} - 6\lambda_{Aegaeon} - \varpi_{Mimas}$) versus time, derived from the numerical integration, showing that it librates about 180°. (b) Fourier spectrum of resonant argument, showing a dominant period of approximately 1260 days and amplitude 10°. (c) Resonant argument of the 7:6 ILR ($\varphi = 7\lambda_{Mimas} - 6\lambda_{Aegaeon} - \varpi_{Aegaeon}$) versus time, showing periods of libration around 0° interspersed with brief periods of circulation. (d) Fourier spectrum of the resonant argument, showing a libration period of approximately 820 days and amplitude of 35°.

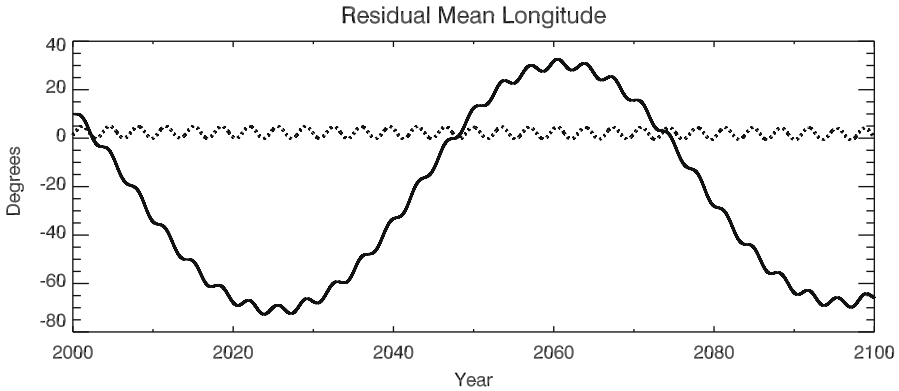

Fig. 9. Aegaeon's residual mean longitude (after removing a constant mean motion of 445.482 deg./day) with and without Tethys included in the integration. Without Tethys, the residual longitude oscillates about zero with an amplitude of about 3°, solely due to the effects of the 7:6 CER with Mimas (dashed curve). The Mimas:Tethys 4:2 resonance causes the additional large amplitude modulation of tens of degrees when Tethys is included in the model (solid curve).

separated by more than 18 km. The forced eccentricity from the Lindblad Resonance is thus larger for Methone than for Aegaeon, which means Aegaeon needs to have a much smaller free eccentricity to be trapped in both resonances than Methone does.

Table 11
Resonant arguments of interest.

Name	Argument	Argument in terms of φ_{CER} and φ_{ILR}
φ_{CER}	$7\lambda_{Mimas} - 6\lambda_{Aegaeon} - \varpi_{Mimas}$	φ_{CER}
φ_{ILR}	$7\lambda_{Mimas} - 6\lambda_{Aegaeon} - \varpi_{Aegaeon}$	$\varphi_{CER} + \varpi_{Mimas} - \varpi_{Aegaeon}$
φ_x	$7\lambda_{Mimas} - 6\lambda_{Aegaeon} + \varpi_{Mimas} - 2\varpi_{Aegaeon}$	$\varphi_{CER} + 2\varpi_{Mimas} - 2\varpi_{Aegaeon} = 2\varphi_{ILR} - \varphi_{CER}$
φ_y	$7\lambda_{Mimas} - 6\lambda_{Aegaeon} - 2\varpi_{Mimas} + \varpi_{Aegaeon}$	$\varphi_{CER} - 2\varpi_{Mimas} + 2\varpi_{Aegaeon} = 2\varphi_{CER} - \varphi_{ILR}$
φ_a	$7\lambda_{Mimas} - 6\lambda_{Aegaeon} - \varpi_{Aegaeon} + \Omega_{Mimas} - \Omega_{Aegaeon}$	$\varphi_{CER} + \varpi_{Mimas} + \Omega_{Mimas} - \varpi_{Aegaeon} - \Omega_{Aegaeon}$ $= \varphi_{ILR} + \Omega_{Mimas} - \Omega_{Aegaeon}$
φ_b	$7\lambda_{Mimas} - 6\lambda_{Aegaeon} - \varpi_{Aegaeon} - \Omega_{Mimas} + \Omega_{Aegaeon}$	$\varphi_{CER} + \varpi_{Mimas} - \Omega_{Mimas} - \varpi_{Aegaeon} + \Omega_{Aegaeon}$ $= \varphi_{CER} + \omega_{Mimas} - \omega_{Aegaeon}$ $= \varphi_{ILR} - \Omega_{Mimas} + \Omega_{Aegaeon}$
φ_c	$7\lambda_{Mimas} - 6\lambda_{Aegaeon} - \varpi_{Mimas} + \Omega_{Mimas} - \Omega_{Aegaeon}$	$\varphi_{CER} + \Omega_{Mimas} - \Omega_{Aegaeon}$
φ_d	$7\lambda_{Mimas} - 6\lambda_{Aegaeon} - \varpi_{Mimas} - \Omega_{Mimas} + \Omega_{Aegaeon}$	$\varphi_{CER} - \Omega_{Mimas} + \Omega_{Aegaeon}$

φ_a–φ_d appear to be examples of secondary resonances, i.e. secular resonances existing inside their respective primary mean motion resonances. The coupling between Aegaeon's eccentricity and inclination mentioned above is also typical of this type of resonant motion (for general discussion of secondary resonant behavior, see Morbidelli (2002)). Of particular interest are the resonant arguments $\varphi_a = \varphi_{CER} + \varpi_{Mimas} + \Omega_{Mimas} - \varpi_{Aegaeon} - \Omega_{Aegaeon}$ and $\varphi_b = \varphi_{CER} + \varpi_{Mimas} - \Omega_{Mimas} - \varpi_{Aegaeon} + \Omega_{Aegaeon}$. The former is equivalent to a resonant argument which was found to be librating for Anthe (ϕ_2 in Cooper et al. (2008)). In Aegaeon, this argument typically stays within ±20° of either 0° or 180°, but can abruptly switch from one state to the other during periods when the eccentricity and inclination are small (see Fig. 10a). To better understand the significance of this behavior, note that φ_{CER} is already approximately constant, and that since $\dot{\varpi}_{Mimas} \simeq -\dot{\Omega}_{Mimas}$, $\varpi_{Mimas} + \Omega_{Mimas}$ is also a constant to good approximation. Therefore, if φ_a remains constant, then $\varpi_{Aegaeon} - \Omega_{Aegaeon}$ must also be constant, which implies that $\dot{\varpi}_{Aegaeon} \simeq -\dot{\Omega}_{Aegaeon}$. This is true for the pericenter precession and nodal regression due to Saturn's oblateness, but is not obviously true for the precession and regression due to perturbations from Mimas. For such perturbations, the Lagrange equations indicate that the pericenter precession rate goes inversely with the eccentricity, while the nodal regression rate goes inversely with the inclination. Thus the only way to have $\dot{\varpi}_{Aegaeon} \simeq -\dot{\Omega}_{Aegaeon}$ is for the eccentricity and inclination to vary in step with one another, which is indeed the case for Aegaeon (see Fig. 7).

φ_b, like φ_a, also exhibits periods of circulation and libration, although its libration amplitude is far greater than for φ_a (see Fig. 10b), suggesting that Aegaeon is located further from the center of this particular resonance. This resonant argument is of particular interest because it can be expressed as $\varphi_b = \varphi_{CER} + \omega_{Mimas} - \omega_{Aegaeon}$. φ_b is therefore the resonant argument of the CER plus the difference in the arguments of pericenter of Mimas and Aegaeon, which suggests that this resonance has some similarities with Kozai Resonances. Although classical Kozai Resonances exist only at high inclinations, Kozai-type secondary resonances can occur inside primary mean motion resonances, even in systems which have small eccentricity and inclination (Morbidelli, 2002). A detailed investigation of the secondary resonances represented by φ_a, φ_b, etc. and their implications for the orbital properties and evolution of Aegaeon is beyond the scope of this paper, but the number of resonant arguments showing interesting behavior indicates that additional work on the detailed orbital properties of this moon should be quite rewarding.

5. Comparisons of moon/ring-arc systems

Aegaeon, like Anthe and Methone, is a small moon embedded in an arc of debris confined by a first-order corotation eccentricity resonance with Mimas. However Aegaeon also appears to be a special case, since it the smallest of these objects while the G-ring arc is brighter than the arcs surrounding the other moons. Thus the

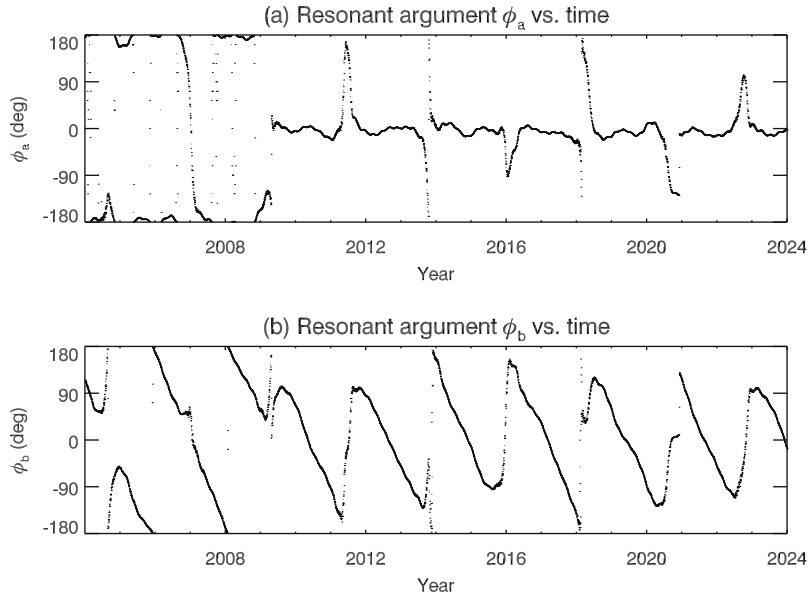

Fig. 10. Resonant arguments $\varphi_a = 7\lambda_{Mimas} - 6\lambda_{Aegaeon} - \varpi_{Aegaeon} - \Omega_{Aegaeon} + \Omega_{Mimas}$ and $\varphi_b = 7\lambda_{Mimas} - 6\lambda_{Aegaeon} - \varpi_{Aegaeon} + \Omega_{Aegaeon} - \Omega_{Mimas}$ versus time, derived from the numerical integration. Note that both these resonant arguments seem to librate around either 0° or 180°.

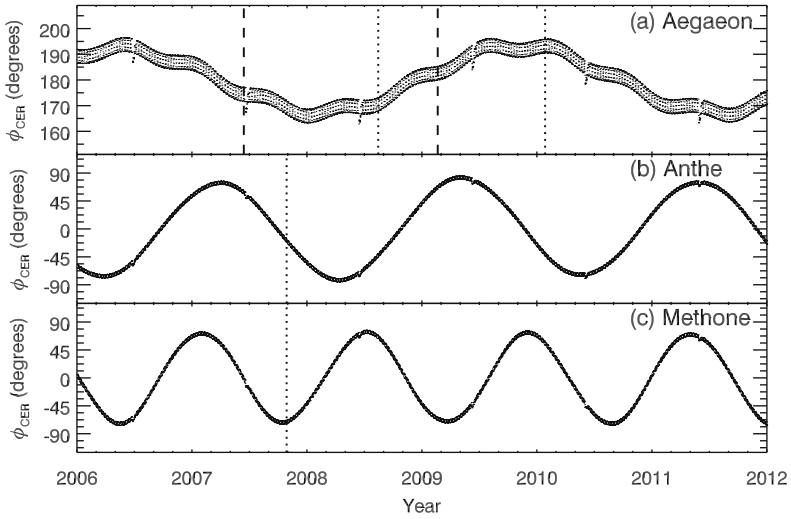

Fig. 11. Corotation eccentricity resonant arguments versus time for Aegaeon, Anthe and Methone. The specific resonant arguments are (a) Aegaeon $\varphi_{CER} = 7\lambda_{Mimas} - 6\lambda_{Aegaeon} - \varpi_{Mimas}$, (b) Anthe $\varphi_{CER} = 11\lambda_{Anthe} - 10\lambda_{Mimas} - \varpi_{Mimas}$, and (c) Methone $\varphi_{CER} = 15\lambda_{Methone} - 14\lambda_{Mimas} - \varpi_{Mimas}$. In (a) coarse vertical dashed lines represent the extent of observational coverage, fine vertical line on the right corresponds to 2010-027 and that on the left to 2008-228. In (b) and (c) vertical dashed lines correspond to 2007-302.

relationship between Aegaeon and the G-ring arc may differ from that between the other moons and their arcs. We therefore compare these systems' dynamical and optical properties.

While Aegaeon, Anthe and Methone are all trapped in corotation eccentricity resonances with Mimas (7:6, 10:11 and 14:15, respectively), their libration amplitudes within those resonances are quite different. As shown in Fig. 11, the libration amplitudes of Anthe and Methone are both between 70° and 80°, while the libration amplitude of Aegaeon is much smaller, only around 10°. Aegaeon is therefore more tightly trapped in its resonance than Anthe and Methone are in theirs.

These differences in the moons' libration amplitudes could explain some of the differences in the gross morphology of the various arcs. These morphological differences are most visible in longitudinal brightness profiles of the arcs' radially integrated brightness, which is expressed in terms of the normal equivalent width:

$$\mathcal{W} = \mu \int (I/F) dr, \tag{7}$$

where μ is the cosine of the emission angle. Note that for low optical depth rings, this quantity (with units of length) is independent of the viewing geometry and the resolution of the images.

Longitudinal brightness profiles of the Anthe and Methone arcs were computed in Hedman et al. (2009), and longitudinal profiles of the G-ring arc are derived in Hedman et al. (2007). However, the Anthe and Methone arc profiles are derived from low-phase-angle (~23°) images, while the published G-ring arc profiles are derived from high-phase-angle (>80°) images, so these published data sets are not truly comparable to each other. Fortunately, the same observations that contain Aegaeon also provide images of the arc at lower phase angles. In particular, the series of images N1597471047–N1597486437 (the sequence in which Aegaeon was first noticed) captured the entire arc at phase angles ~28°, which is comparable to the phase angles of the Anthe and Methone arc observations. A longitudinal brightness profile of the G-ring arc was derived from these images following procedures similar to those used in Hedman et al. (2007, 2009). First, the relevant imaging data were re-projected onto a grid of radii and longitudes relative to the predicted location of Aegaeon. To isolate the arc signal from the rest of the ring, a radial brightness profile of the background G-ring was computed by averaging the data over longitudes between −40° and −50° from Aegaeon, where the arc signal was absent. After subtracting this background, the normal equivalent width at each longitude was computed by integrating the brightness over the radial range of 167,000–168,000 km.

Fig. 12 displays the longitudinal brightness profiles of the various arcs. Note the x-axis on these plots is the resonant argument φ of the appropriate corotation eccentricity resonances instead of actual longitudes, so that the curves can be compared more easily. Intriguingly, the G-ring profile has a distinct peak near $\varphi = 0$, while the Anthe arc is broad with a nearly constant brightness over a broad range of longitudes. In all likelihood, this difference in the morphology of the arcs is directly related to the differences in the moons' libration amplitudes described above. Aegaeon has a relatively small libration amplitude, and so never strays far from $\varphi = 0$, while Anthe has a large libration amplitude and thus moves through a wider range of longitudes within the pocket containing the particles. Thus we might expect that material shed from Anthe would be more evenly distributed in longitude than the material derived from Aegaeon. Furthermore, Anthe should be better able to stir and scatter debris throughout the arc as it moves back and forth through the arc.

The Methone arc presents a more complicated situation, since the amplitude of Methone's libration is comparable to Anthe's, but its arc is not as wide. This could possibly be attributed to the fact that Methone occupies both the 14:15 corotation resonance and the 14:15 Lindblad Resonance, and so the dynamics of the particles in this region may be more complicated than those in the Anthe arc.

In addition to the differences in the morphology of the arcs associated with the various moons, the arcs' overall brightnesses show some interesting trends. In analogy to the normal equivalent width given above, one can define a normal equivalent area $\mathcal{A}$ as the total integrated brightness of a ring over radius and longitude λ:

$$\mathcal{A} = r_o \int \mathcal{W} d\lambda, \tag{8}$$

where r_o is the effective mean radius of the ring. Note that this quantity has units of area and provides a measure of the total surface area of material in the ring.

Integrating each arc's equivalent width over all longitudes (and interpolating the Anthe and Methone arcs over the region dominated by the signal from the moons), we obtain normal equivalent

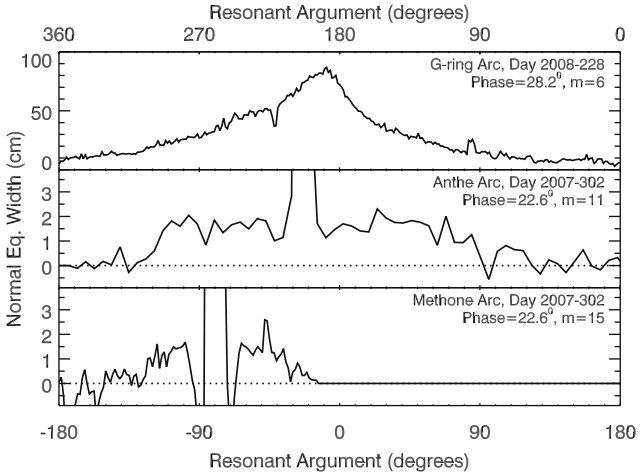

Fig. 12. Longitudinal profiles of the arcs in the G-ring (top), Anthe ring (middle) and Methone ring (bottom). Each profile shows the normal equivalent width of the arc versus the appropriate resonant argument of the appropriate corotation resonance. Note the top axis refers to the G-ring arc (which is interior to Mimas) while the bottom axis refers to both the Anthe and Methone arcs (both of which are exterior to Mimas). In all cases, the right sides of the plots lead the relevant moons.

areas of the G-ring, Anthe and Methone arcs of 50, 1.0 and 0.3 km^2, respectively. The G-ring arc's integrated brightness is therefore about 2 orders of magnitude higher than the arcs associated with Anthe and Methone. This difference becomes more striking if we compare these numbers to the effective areas of the moons at comparable phase angles. Inserting the values in Table 5 into Eq. (5), we find that the effective areas of Aegaeon, Anthe and Methone at 25° phase are 0.07, 0.84 and 2.21 km^2. For Anthe and Methone, the normal equivalent areas of the arcs are comparable to the effective area of the moons, which implies that the debris in these arcs have comparable surface areas as the moons. Since the particles in the arcs are likely significantly smaller than the moons, this means that the mass in the Anthe and Methone arcs are much less than the mass in the moons themselves. By contrast, the normal equivalent area of the G-ring arc is between 10^3 and 10^4 times the effective area of Aegaeon.

Most of the visible material in the faint rings likely originates from clouds of debris knocked off the larger particles and moons by micrometeoroids, so one possible explanation for the distinctive characteristic of the Aegaeon/G-ring system is that Aegaeon is more efficient at generating dust than the larger moons Anthe and Methone. Smaller moons do have lower surface gravity, so a given micrometeoroid impact will yield a larger fraction of ejecta that will escape into the ring. However, smaller moons also have lower cross-sections and thus have lower impact rates, and theoretical calculations suggest that the optimal moon size for dust production is around 10 km (Burns et al., 1984, 1999). Even though this optimal size depends on the assumed surface properties of the source bodies, it is larger than any of the moons considered here, so this model predicts that Aegaeon would actually be less efficient at generating dust than Anthe or Methone.

An alternative explanation arises from the realization that the normal equivalent area of the G-ring and the arc are orders of magnitude higher than the physical area of Aegaeon, which is not the case for any of the other ring–moon systems. Aegaeon therefore does not dominate the cross-section of its ring to the same extent as the other moons, so it is quite likely that Aegaeon shares the arc with a number of other objects 1–100 m across that act as additional sources of the visible G-ring. Such objects would be difficult to see in the available images because they would be smeared out into streaks by the long exposure times, which makes them hard to detect against the background brightness of the G-ring arc. However, in situ measurements provide evidence that additional source bodies do reside in the G-ring arc. Using in situ data from the Voyager spacecraft, van Allen (1983) computed the total cross-sectional area of large (>10 cm) particles in the G-ring to be 20 km^2. This is comparable to the normal equivalent area of the arc derived above and is much larger than the area of Aegaeon, implying that there is indeed a significant population of large objects in the vicinity of the G-ring. More recently, the MIMI instrument onboard Cassini detected a ~250-km wide electron microsignature associated specifically with the G-ring arc. The depth of this microsignature required a total mass of material equivalent to a roughly 100-m wide ice-rich moonlet, orders of magnitude greater than the mass in dust-sized grains inferred from images (Hedman et al., 2007). Furthermore, the signature is too wide to be explained by a single moon like Aegaeon, which suggests that the arc contains a substantial population of electron-absorbing source bodies. The G-ring arc therefore appears to contain debris with a broad range of sizes, perhaps the remains of a shattered moon, while the Anthe and Methone arcs are just the latest small particles knocked off of the relevant moons.

If Aegaeon does share the G-ring arc with a population of source bodies 1–100 m across, this could influence its dynamics. As Aegaeon librates within the arc, it will collide with these smaller objects. Collisions within dense arcs of debris confined by corotation resonances are expected to increase the libration amplitudes of particles and ultimately allow them to escape the resonance because collisions dissipate energy and the stable points of corotation resonances are potential energy maxima (Porco, 1991; Namouni and Porco, 2002). However, this situation is slightly different, because we have a single large body moving through a sea of smaller bodies that should have no average net velocity relative to the stable point of the resonance. Hence collisions will act against any motion of Aegaeon relative to the resonance, and therefore cause Aegaeon's free inclination, free eccentricity, and libration amplitude to decay over time.

A crude estimate of the dissipation timescales due to collisions can be computed by assuming an object of radius R and mass M moves at a velocity v through a background medium consisting of a population of small particles. Say the mass density of the background medium is ρ_b, then the mass encountered by the object in a time dt is $\rho_b \pi R^2 v dt$. The momentum imparted to this material is $C\rho_b \pi R^2 v^2 dt$, where C is a dimensionless constant of order unity. This must equal the corresponding decrease in the momentum of the object Mdv, so the acceleration of the object due to collisions with the medium is given by:

$$\frac{dv}{dt} = \frac{C\rho_b \pi R^2 v}{M} v. \tag{9}$$

Assuming the object has an initial velocity v_i at time $t = 0$, the velocity will decay with time as follows:

$$v(t) = v_i \left(1 + \frac{C\pi\rho_b R^2 v_i}{M} t\right)^{-1}. \tag{10}$$

Thus the characteristic timescale over which the velocity falls by a factor of 1/2 is:

$$t_c = \frac{1}{C\pi R^2 v_i} \frac{M}{\rho_b}. \tag{11}$$

Now, since the mass density of the medium (i.e. the arc) is the most uncertain variable, let us re-express that parameter in terms of the arc's mass m_a and its spatial volume V_a.

$$t_c = \frac{1}{C} \frac{M}{m_a} \frac{V_a}{\pi R^2 v_i}. \tag{12}$$

We may now attempt to estimate this characteristic timescale for moons like Aegaeon and Anthe. Libration amplitudes of $\sim 10^\circ$ and finite eccentricities of $\sim 10^{-3}$ (both reasonable for moons like Aegaeon or Anthe) lead to typical velocities relative to the resonance's stable point of order 1 m s^{-1}. The G-ring arc has a longitudinal extent of $\sim 20^\circ$ or $\sim 6 \times 10^4$ km and a radial width of ~ 250 km (Hedman et al., 2007). Assuming its vertical thickness is comparable to its radial width, the volume of the G-ring arc is of order 4×10^{18} m^3. Inserting these numbers into Eq. (12), the critical timescale can be expressed as follows:

$$t_c \simeq \frac{6 \times 10^5 \text{ years}}{C} \frac{M}{m_a} \left(\frac{V_a}{4 \times 10^{18} \text{ m}^3} \right) \left(\frac{250 \text{ m}}{R} \right)^2 \left(\frac{1 \text{ m/s}}{v_i} \right), \qquad (13)$$

where all of the terms in parentheses should be of order unity for Aegaeon.

Assuming that Aegaeon has a mass density of about 0.5 g/cm^3, its mass would be $M \simeq 3 \times 10^{10}$ kg. Based on the depth of an electron microsignature observed in the arc's vicinity, Hedman et al. (2007) estimated that the arc's total mass was between 10^8 and 10^{10} kg (the width of the microsignature was more consistent with it being associated with the arc than with the moon). We can therefore estimate m_a/M to be between 0.003 and 0.3, which would imply damping timescales between 10^6 and 10^8 years. By contrast, Anthe's radius is four times larger than Aegaeon's, so its mass is ~ 64 times larger than Aegaeon's. Furthermore, assuming the total integrated brightness scales with the total mass, then the mass of the Anthe arc is at least ~ 50 times smaller than that of the G-ring arc. The characteristic damping time for Anthe should therefore be at least ~ 200 times longer than for Aegaeon, or 10^8–10^{10} years.

Anthe's characteristic damping time is comparable to the age of the Solar System, which implies that collisional damping has had relatively little effect on Anthe's orbit. Aegaeon's characteristic damping time is much shorter, so collisional damping may be significant for this moon. However, the above values for the damping time will only apply as long as the moon and the arc have their present masses. Since hypervelocity impacts with objects on heliocentric orbits will steadily erode or fragment small moons (cf. Colwell et al., 2000), it is likely that Aegaeon was larger in the past than it is today. Thus collisional damping can only be effective on Aegaeon if its collision damping time is less than the appropriate erosion or fragmentation timescale.

In lieu of a detailed analysis of Aegaeon's fragmentation history, we can roughly estimate how long Aegaeon may have had its current size by computing the frequency of catastrophic impacts into the moon. The specific energy required for catastrophic fragmentation (i.e. the largest remaining fragment is less than one-half the mass of the original target) of an ice-rich object is of order 2×10^5 erg/g (Giblin et al. (2004), see also sources cited in Colwell et al. (2000)). Assuming typical impact velocities of order 40 km s^{-1}, this means catastrophic fragmentation will occur when the ratio of the impactor's mass to the moon's mass is above about 2.5×10^{-8}. If we again assume that Aegaeon has a mass of about 3×10^{10} kg, then any impactors with a mass more than 1000 kg would be able to catastrophically disrupt the moon. The present flux of such objects is quite uncertain, but 10^{-20}/m^2/s is consistent with previous estimates and extrapolations (Ip, 1984; Colwell and Esposito, 1992). This flux gives a catastrophic impact rate into a 500-m wide Aegaeon of order 1 per 10^7 years. This is comparable to the characteristic damping time derived above, so these calculations indicate that Aegaeon could have been close to its present size over a long enough period of time for collisional damping to significantly change its orbit. Clearly, more detailed analyses are needed to clarify and quantify the possible interactions between Aegaeon and the G-ring arc, but these rough calculations do suggest that collisional damping could provide a reasonable explanation for Aegaeon's distinctive dynamical properties.

6. Conclusions

Even though the currently available data on Aegaeon are sparse, they are sufficient to demonstrate that it is a interesting object worthy of further investigation. With a photometrically estimated diameter of less than a kilometer, Aegaeon is the smallest isolated moon of Saturn yet observed, and may be comparable in size to the largest particles in Saturn's main rings, which form the so-called "giant-propellers" in the A ring (Tiscareno et al., 2009). Aegaeon occupies a corotation eccentricity resonance with Mimas, like Anthe and Methone, and all three of these moons are associated with resonantly-confined arcs of debris. However, Aegaeon also appears to be a special case in terms of its orbital properties and its relationship with its arc. Its eccentricity and inclination are both extremely low, and the large number of resonant arguments on the boundary between circulation and libration lead to some interesting dynamical behavior. At the same time, the mass in the G-ring arc is probably a significant fraction of (and may even be comparable to) Aegaeon's mass, unlike the other arcs associated with small moons, opening up the possibility that interactions between the moon and the material in the arc could be responsible for some of Aegaeon's unusual orbital characteristics. Future analysis of this system could therefore provide insights into the orbital evolution of satellites coupled to disks of debris.

Acknowledgments

We thank P.D. Nicholson and J. Veverka for useful conversations, and we also wish to thank two anonymous reviewers for their comments on earlier versions of this manuscript. We acknowledge the support of NASA, the Cassini Project and the Imaging Team. We also wish to thank the VIMS team, who designed several of the observations discussed here. N.C., C.M., K.B. and M.E. acknowledge the financial support of the UK Science and Technology Facilities Council.

References

Acton, C.H., 1996. Ancillary data services of NASA's Navigation and Ancillary Information Facility. Planet. Space Sci. 44, 65–70.
Borderies, N., Longaretti, P.-Y., 1994. Test particle motion around an oblate planet. Icarus 107, 129–141.
Bowell, E., Lumme, K., 1979. Colorimetry and magnitudes of asteroids. In: Gehrels, T. (Ed.), Asteroids. University of Arizona Press, pp. 132–169.
Brankin, R., Gladwell, L., Dormand, J., Prince, P., Seward, W., 1989. A Runge–Kutta–Nyström code. ACM Trans. Math. Software 15, 31–40.
Burns, J.A., Showalter, M.R., Hamilton, D.P., Nicholson, P.D., de Pater, I., Ockert-Bell, M.E., Thomas, P.C., 1999. The formation of Jupiter's faint rings. Science 284, 1146–1150.
Burns, J.A., Showalter, M.R., Morfill, G.E., 1984. The ethereal rings of Jupiter and Saturn. In: Greenberg, R., Brahic, A. (Eds.), Planetary Rings. University of Arizona Press, pp. 200–272.
Colwell, J.E., Esposito, L.W., 1992. Origins of the rings of Uranus and Neptune. I – Statistics of satellite disruptions. J. Geophys. Res. 97, 10227–10241.
Colwell, J.E., Esposito, L.W., Bundy, D., 2000. Fragmentation rates of small satellites in the outer Solar System. J. Geophys. Res. 105, 17589–17600.
Cooper, N.J., Murray, C.D., 2004. Dynamical influences on the orbits of Prometheus and Pandora. Astron. J. 127, 1204–1217.
Cooper, N.J., Murray, C.D., Evans, M.W., Beurle, K., Jacobson, R.A., Porco, C.C., 2008. Astrometry and dynamics of Anthe (S/2007 S4), a new satellite of Saturn. Icarus 195, 765–777.
Giblin, I., Davis, D.R., Ryan, E.V., 2004. On the collisional disruption of porous icy targets simulating Kuiper belt objects. Icarus 171, 487–505.
Hedman, M.M., Burns, J.A., Tiscareno, M.S., Porco, C.C., Jones, G.H., Roussos, E., Krupp, N., Paranicas, C., Kempf, S., 2007. The source of Saturn's G-ring. Science 317, 653–657.
Hedman, M.M., Murray, C.D., Cooper, N.J., Tiscareno, M.S., Beurle, K., Evans, M.W., Burns, J.A., 2009. Three tenuous rings/arcs for three tiny moons. Icarus 199, 378–386.

Ip, W., 1984. Ring torque of Saturn from interplanetary meteoroid impact. Icarus 60, 547–552.
Jacobson, R.A., 2004. The orbits of the major saturnian satellites and the gravity field of Saturn from spacecraft and Earth-based observations. Astron. J. 128, 492–501.
Kliore, A.J., Patel, I.R., Lindal, G.F., Sweetnam, D.N., Hotz, H.B., Waite, J.H., McDonough, T., 1980. Structure of the ionosphere and atmosphere of Saturn from Pioneer 11 Saturn radio occultation. J. Geophys. Res. 85, 5857–5870.
Kozai, Y., 1962. Secular perturbations of asteroids with high inclination and eccentricity. Astron. J. 67, 591–598.
Morbidelli, A., 2002. Modern Celestial Mechanics: Aspects of Solar System Dynamics. Taylor and Francis.
Murray, C.D., Cooper, N.J., Evans, M.W., Beurle, K., 2005. S/2004 S5: A new co-orbital companion for Dione. Icarus 179, 222–234.
Namouni, F., Porco, C., 2002. The confinement of Neptune's ring arcs by the moon Galatea. Nature 417, 45–47.
Nicholson, P.D., Porco, C.C., 1988. A new constraint on Saturn's zonal gravity harmonics from Voyager observations of an eccentric ringlet. J. Geophys. Res. 93, 10209–10224.
Porco, C.C., 1991. An explanation for Neptune's ring arcs. Science 253, 995–1001.
Porco, C.C., and 34 colleagues, 2005. Cassini imaging science: Initial results on Saturn's rings and small satellites. Science 307, 1226–1236.
Porco, C.C., on behalf of the Cassini Imaging Team, 2009. S/2008 S1. IAU Circ. 9023.
Porco, C.C., Thomas, P.C., Weiss, J.W., Richardson, D.C., 2007. Saturn's small inner satellites: Clues to their origins. Science 318, 1602–1607.
Porco, C.C., and 19 colleagues, 2004. Cassini imaging science: Instrument characteristics and anticipated scientific investigations at Saturn. Space Sci. Rev. 115, 363–497.
Renner, S., 2004. Dynamique des anneaux et des satellites planetaires: Application aux arcs de Neptune et au systeme Promethee-Pandore. Ph.D. Thesis, L'Observatoire de Paris.
Renner, S., Sicardy, B., 2006. Use of the geometric elements in numerical simulations. Celest. Mech. Dynam. Astron. 94, 237–248.
Roussos, E., Jones, G.H., Krupp, N., Paranicas, C., Mitchell, D.G., Krimigis, S.M., Woch, J., Lagg, A., Khurana, K., 2008. Energetic electron signatures of Saturn's smaller moons: Evidence of an arc of material at Methone. Icarus 193, 455–464.
Spitale, J.N., Jacobson, R.A., Porco, C.C., Owen Jr., W.M., 2006. The orbits of Saturn's small satellites derived from combined historic and Cassini imaging observations. Astron. J. 132, 692–710.
Tiscareno, M.S., Burns, J.A., Beurle, K., Spitale, J., Cooper, N.J., Porco, C.C., 2009. Giant propellers outside the Encke gap in Saturn's rings. Bulletin of the American Astronomical Society, vol. 41. Bulletin of the American Astronomical Society, p. 559.
van Allen, J.A., 1983. Absorption of energetic protons by Saturn's ring G. J. Geophys. Res. 88, 6911–6918.
Veverka, J., 1971. The physical meaning of phase coefficients. NASA Spec. Publ. 267, 79–90.
Veverka, J., 1977. Photometry of satellite surfaces. In: Burns, J.A. (Ed.), Planetary Satellites. University of Arizona Press, pp. 171–209.
Vienne, A., Duriez, L., 1995. TASS1.6: Ephemerides of the major saturnian satellites. Astron. Astrophys. 297, 588–605.